

An X-ray study of magnetic field strengths and particle content in the lobes of FR II radio sources

J.H. Croston^{1,4}, M.J. Hardcastle^{2,4}, D.E. Harris³, E. Belsole⁴, M. Birkinshaw⁴ and D.M. Worrall⁴

ABSTRACT

We present a *Chandra* and *XMM-Newton* study of X-ray emission from the lobes of 33 classical double radio galaxies and quasars. We report new detections of lobe-related X-ray emission in 11 sources. Together with previous detections we find that X-ray emission is detected from at least one radio lobe in ~ 75 percent of the sample. For all of the lobe detections, we find that the measured X-ray flux can be attributed to inverse-Compton scattering of the cosmic microwave background radiation, with magnetic field strengths in the lobes between $(0.3 - 1.3) B_{eq}$, where the value B_{eq} corresponds to equipartition between the electrons and magnetic field assuming a filling factor of unity. There is a strong peak in the magnetic field strength distribution at $B \sim 0.7 B_{eq}$. We find that > 70 percent of the radio lobes are either at equipartition or electron dominated by a small factor. The distribution of measured magnetic field strengths differs for narrow-line and broad-line objects, in the sense that broad-line radio galaxies and quasars appear to be further from equipartition; however, this is likely to be due to a combination of projection effects and worse systematic uncertainty in the X-ray analysis for those objects. Our results suggest that the lobes of classical double radio sources do not contain an energetically dominant proton population, because this would require the magnetic field energy density to be similar to the electron energy density rather than the overall energy density in relativistic particles.

¹Service d'Astrophysique, CEA Saclay, L'Orme des Merisiers, 91191 Gif-sur-Yvette, France.
Email: jcroston@discovery.saclay.cea.fr

²School of Physics, Astronomy and Mathematics, University of Hertfordshire, College Lane, Hatfield AL10 9AB, UK

³Harvard-Smithsonian Center for Astrophysics, 60 Garden Street, Cambridge, MA 02138, USA

⁴Department of Physics, University of Bristol, Tyndall Avenue, Bristol BS8 1TL, UK

Subject headings: galaxies: active – X-rays: galaxies – X-rays: quasars – radiation mechanisms: non-thermal

1. Introduction

Detections of X-ray inverse-Compton emission from components of radio galaxies have the potential to resolve long-standing questions about their particle content and magnetic field strength, because they allow direct measurements of electron energy density, unlike observations of radio synchrotron emission, where the electron density and magnetic field strength cannot be decoupled. This technique has been successfully used to measure magnetic field strengths in the hotspots and lobes of FR II (Fanaroff and Riley 1974) radio galaxies and quasars. Measurements of the internal energy density in relativistic electrons obtained from X-ray lobe detections can be used to constrain source dynamics and particle content by allowing a comparison of the internal pressure with the external pressure from X-ray-emitting hot gas (e.g., Hardcastle et al. 2002; Croston et al. 2004). This is particularly important in view of the continuing uncertainty about the dynamical status and confinement of FR II lobes (Hardcastle and Worrall 2000).

There are several possible sources of photons to be inverse-Compton scattered up to X-ray energies by the radio-synchrotron-emitting electron population. In hotspots, where the electron density is high, the dominant photon population comes from the radio emission itself; this is the synchrotron-self Compton process (Hardcastle et al. 2004). However, in the lobes the density of synchrotron photons is much lower, so that the photon energy density from the cosmic microwave background typically dominates over that from the radio synchrotron emission. In addition, the photon field from the nuclear source may be important in some sources (Brunetti et al. 1997). *Chandra* and *XMM-Newton* have allowed a number of detections of X-ray emission from lobes to be made. In many sources the lobes have been claimed to be near to equipartition (e.g., Hardcastle et al. 2002; Belsole et al. 2004; Croston et al. 2004; Bondi et al. 2004; Overzier et al. 2005) whereas in others significant electron dominance is claimed (e.g., Isobe et al. 2002; Comastri et al. 2003; Kataoka et al. 2003b). However, the results are dependent on the assumed electron energy spectrum and photon population characteristics. The unknown properties of the electron population at energies below those observable in the radio also introduce considerable uncertainty (e.g., Harris 2004). Differences in the methods used to separate thermal and non-thermal X-ray emission, and in the calculations of inverse-Compton emissivity can also be important, so that estimates from different authors are often not directly comparable. As yet there is no overall picture of the magnetic field properties of the FR II population.

The particle content in radio galaxies and quasars has been the subject of debate over several decades. There are arguments in favor of electron-proton jets, principally based on energy transport close to the active nucleus (e.g., Celotti and Fabian 1993); however, several independent arguments favor electron-positron jets (e.g. Wardle et al. 1998; Homan and Wardle 1999; Kino and Takahara 2004). Inverse-Compton studies can provide indirect information on the particle content on the large scale: although relativistic protons are not directly observable by this process, inverse-Compton observations that are consistent with equipartition between the magnetic field and electron energy densities make it difficult to accommodate an energetically dominant population of protons in the lobes. Hardcastle et al. (2004) have already used this argument to suggest that hotspot energetics are not dominated by protons, and Hardcastle et al. (2002) and Croston et al. (2004) have applied it to individual FR II lobes; extending it to FR II lobes in general would be of considerable interest.

In this paper we use the *Chandra* archives (together with some *XMM-Newton* data) to compile a large sample of FR II radio galaxies and quasars with which to investigate the inverse-Compton properties of lobes. Our approach differs from that of Kataoka and Stawarz (2005) in that we do not only select sources with known hotspot, jet or lobe emission, but include sources whose extended components have not previously been detected in X-rays: this allows us to consider limits on the magnetic field strength, and gives us a much larger sample (as well as allowing us to make some new lobe detections). In Section 4, we compare our results with theirs. Throughout the paper we use a cosmology in which $H_0 = 70 \text{ km s}^{-1} \text{ Mpc}^{-1}$, $\Omega_m = 0.3$ and $\Omega_\Lambda = 0.7$. Spectral indices α are the energy indices and are defined in the sense $S_\nu \propto \nu^{-\alpha}$.

2. Sample and data analysis

2.1. Sample

The sample was compiled from the list of 3C FR II radio sources for which public *Chandra* observations existed as of early 2004, which comprises 36 objects (Hardcastle et al. 2004). We also included 4 *XMM-Newton* observations of 3C radio galaxies for which detailed analysis of lobe-related emission has previously been carried out (Belsole et al. 2004; Croston et al. 2004). This gave a total sample size of 40 objects, which span a redshift range of $\sim 0.05 - 2$. In Table 1, the full sample is listed, together with details of the observations and references to previously published work.

Table 1. The sample of X-ray observed FR II radio sources.

Source	z	Type	α_R	OBS	Obsid	Date observed	Duration (s)	Reference
3C 6.1	0.8404	N	0.68	C	3009	2002 Oct 15	36492	2
3C 9	2.012	Q	1.12	C	1595	2001 Jun 10	19883	1
3C 47	0.425	Q	0.98	C	2129	2001 Jan 16	44527	2
3C 109	0.306	B	0.85	C	4005	2003 Mar 23	45713	2
3C 123	0.2177	E	0.70	C	829	2000 Mar 21	38465	14
3C 173.1	0.292	E	0.88	C	3053	2002 Nov 06	23999	2
3C 179	0.846	Q	0.73	C	2133	2001 Jan 15	9334	3
3C 184	0.994	N	0.86	C	3226	2002 Sep 22	18886	4 ^a
3C 200	0.458	N	0.84	C	838	2000 Oct 06	14660	
3C 207	0.684	Q	0.90	C	2130	2000 Nov 04	37544	5
3C 212	1.049	Q	0.92	C	434	2000 Oct 26	18054	15
3C 215	0.411	Q	1.06	C	3054	2003 Jan 02	33803	2
3C 219	0.1744	B	0.81	C	827	2000 Oct 11	17586	6
3C 220.1	0.61	N	0.93	C	839	1999 Dec 29	18922	16
3C 223	0.1368	N	0.74	X	0021740101	2003 May 30	34000	7 ^a
3C 228	0.5524	N	1.0	C	2453	2001 Apr 23	13785	
3C 254	0.734	Q	0.96	C	2209	2001 Mar 26	29668	17
3C 263	0.652	Q	0.82	C	2126	2000 Oct 28	44148	8 ^b
3C 265	0.8108	N	0.96	C	2984	2002 Apr 25	58921	9
3C 275.1	0.557	Q	0.96	C	2096	2001 Jun 02	24757	10
3C 280	0.996	N	0.81	C	2210	2001 Aug 27	63528	17
3C 281	0.602	Q	0.71	C	1593	2001 May 30	15851	10
3C 284	0.2394	N	0.95	X	0021740201	2002 Dec 12	43000	7 ^a
3C 292	0.710	N	0.80	X	0147540101	2002 Oct 29	34000	4 ^a
3C 294	1.78	N	1.07	C	3207	2002 Feb 27	122020	11 ^c
3C 295	0.4614	N	0.63	C	2254	2001 May 18	90936	18
3C 303	0.141	B	0.76	C	1623	2001 Mar 23	14951	19
3C 321	0.096	N	0.60	C	3138	2002 Apr 30	47130	2
3C 322	1.681	N	0.81	X	0028540301	2002 May 17	43000	4 ^a
3C 324	1.2063	N	0.90	C	326	2000 Jun 25	42147	2
3C 330	0.5490	N	0.71	C	2127	2001 Oct 16	44083	8 ^b

Table 1—Continued

Source	z	Type	α_R	OBS	Obsid	Date observed	Duration (s)	Reference
3C 334	0.555	Q	0.86	C	2097	2001 Aug 22	32468	
3C 351	0.371	Q	0.73	C	2128	2001 Aug 24	45701	8 ^b
3C 390.3	0.0569	B	0.75	C	830	2000 Apr 17	33974	
3C 401	0.201	E	0.71	C	3083	2002 Jul 20	22666	20
3C 403	0.0590	N	0.74	C	2968	2002 Dec 07	49472	12 ^a
3C 405	0.0590	N	0.74	C	360	2000 May 21	34720	21
3C 427.1	0.572	E	0.97	C	2194	2002 Jan 27	39456	
3C 438	0.290	E	0.88	C	3967	2002 Dec 27	47272	
3C 452	0.0811	N	0.78	C	2195	2001 Aug 21	79922	13

Note. — Column 3 gives the radio-source type: N is a narrow-line radio galaxy, B is a broad-line radio galaxy, E is a low-excitation radio galaxy, and Q is a radio-loud quasar. Column 4 gives the low-frequency radio spectral index (normally between 178 and 750 MHz). Column 5 indicates whether the observation was with *Chandra* (C) or *XMM-Newton* (X). Column 6 gives the *Chandra* or *XMM-Newton* observing ID. Columns 7 and 8 give the observing date and original livetime. References for observations already discussed in the literature are in column 9.

References. — (1) Fabian et al. 2003; (2) Hardcastle et al. 2004; (3) Sambruna et al. 2002; (4) Belsole et al. 2004; (5) Brunetti et al. 2002; (6) Comastri et al. 2003; (7) Croston et al. 2004; (8) Hardcastle et al. 2002; (9) Bondi et al. (2003); (10) Crawford and Fabian 2003; (11) Crawford et al. 2003; (12) Kraft et al. (2005); (13) Isobe et al. 2002; (14) Hardcastle et al. 2001; (15) Aldcroft et al. 2003; (16) Worrall et al. 2001; (17) Donahue et al. 2003; (18) Brunetti et al. 2001; (19) Kataoka et al. 2003a; (20) Reynolds et al. 2004; (21) Wilson et al. 2000.

^aThe authors’ analysis methods are similar to those used in the current paper, so we do not reanalyse this observation.

^bThe authors’ analysis methods are similar to those used in the current paper, but we repeat their inverse-Compton calculations to take into account a different cosmology and low-energy

electron cutoff.

^cThe authors argue that there is IC emission produced by scattering of CMB photons around this high redshift source; however, the emission is not coincident with the lobes or any detected radio emission, so this is not an X-ray lobe detection by our definition.

2.2. X-ray analysis

Nine of the sources in the sample have previous detections of lobe-related emission analysed by workers including a subset of the present authors, with analysis based around the SYNCH code of Hardcastle et al. (1998a). Of the remaining objects, six have previously published detections of lobe-related X-ray emission. For consistency with the rest of our sample, we reanalysed the data for those lobe detections that had not previously been analysed using our code.

We extracted the *Chandra* archive data for the 31 objects not previously studied by our group, and prepared and analysed the data using standard methods using CIAO 3.1 and CALDB 2.28. The data were filtered for good time intervals, and an image in the energy range 0.5 – 5.0 keV was made for each source. We examined the X-ray image to determine whether it would be possible to make a measurement of the lobe-related X-ray emission. In 7 cases, we decided that it would be impossible to determine accurately the level of X-ray emission associated with the radio lobes, either because of background-subtraction difficulties or other confusing components of X-ray emission. These cases were 3C 123, 3C 295, 3C 401, 3C 405 and 3C 438, which are all in rich clusters that in several cases show complex structure on the scales of the radio lobes; 3C 294, where extended non-thermal X-ray emission, not associated with the lobes, is present (Crawford et al. 2003); and 3C 324, where hotspot-lobe separation would be difficult (Hardcastle et al. 2004). In addition, there were several sources where it was only possible to determine the level of lobe-related X-ray emission accurately for one of the two lobes, because of confusion with bright AGN, jet or hotspot emission. The sources for which only one lobe could be studied are 3C 9, 3C 207, 3C 212, 3C 254, 3C 280, 3C 303, and 3C 321. In total, the analysis was carried out for 24 radio galaxies and quasars, which, together with the 9 previously studied objects, gives a total sample of 54 lobes.

Spectral extraction regions were chosen based on the extent of the radio structure, as determined using the 1.4-GHz radio maps (see the following Section). The regions are circular, rectangular or elliptical approximations to the extent of low-frequency radio emission. In all but two cases spectra were obtained separately for each radio lobe. Low-frequency radio maps were used as they best represent the distribution of the electrons responsible for scattering CMB photons to X-ray energies. In most cases the lobe-related emission is of extremely low surface brightness, so that accurate background subtraction is crucial. In many cases there is also X-ray emission from a bright AGN and from the hot-gas environment. We therefore used local background regions at the same distance from the core as the source regions, so as to minimize the contamination, which is expected to be symmetrically distributed, and in particularly difficult cases (strong nuclear X-ray emission and small

lobes) used PSF modelling based on CHART¹ and MARX to verify the correctness of our extraction regions. Spectral extraction was carried out using the CIAO task PSEXTRACT, which produces source and background spectra and response files (we compared our results with those obtained using weighted response files generated using the ACISSPEC script for several representative sources and found no significant differences; we therefore chose to use the considerably faster PSEXTRACT script). We used the energy range 0.5 – 5.0 keV for spectral analysis.

Where there were sufficient counts, the spectrum was grouped to a minimum of 20 counts per background-subtracted bin, and a power-law model was fitted to the extracted spectrum using XSPEC. In all cases Galactic N_{H} was assumed, using values from pointed observations or obtained with the N_{H} tool provided by NASA’s High Energy Astrophysics Science Archive Research Center (HEASARC)², based on the measurements of Dickey and Lockman (1990). In the case of 3C 452, where subtraction of any thermal emission was difficult due to the radio-source morphology, we also fitted a two-component *mekal* plus power-law model. In the majority of cases, however, the total number of background-subtracted counts was too low to fit a spectrum or there was no detected X-ray emission above the 3σ background level. In those cases, we assumed a power-law photon spectrum with $\Gamma = 1.5$, and used the measured count rate, or upper limit from the 3σ background level, to determine the 1-keV flux density. Table 2 gives details of the spectral fits for those sources where it was possible to fit the spectrum. In most cases an acceptable fit is obtained for $\Gamma = 1.5$, as expected for inverse-Compton emission by radio-synchrotron-emitting electrons with the typical injection energy spectrum predicted from shock acceleration (e.g. Bell 1978). Table 3 gives the absorbing column density, number of counts and flux density measurements for the other detected sources, and Table 4 gives upper limits for the remaining sources.

¹See <http://cxc.harvard.edu/chart/> .

²<http://heasarc.gsfc.nasa.gov/>

Table 2. Spectral fits for X-ray lobe detections with sufficient counts.

Source	Net counts	N_{H} (cm^{-2})	Γ	$S_{1 \text{ keV}}$ (nJy)	$\chi^2/\text{d.o.f.}$
3C 47N	197	5.87×10^{20}	1.4 ± 0.4	3.6 ± 0.7	4.9/6
3C 47S	434	5.87×10^{20}	1.9 ± 0.2	10 ± 1	21/15
3C 215N	109	3.75×10^{20}	1.4 ± 0.3	2.9 ± 0.4	1/3
3C 215S	119	3.75×10^{20}	1.5 ± 0.5	2.9 ± 0.5	2.9/3
3C 219N	188	1.51×10^{20}	2.0 ± 0.3	9 ± 1	3.6/6
3C 219S	147	1.51×10^{20}	1.7 ± 0.5	7 ± 1	7/4
3C 265E	142	1.90×10^{20}	1.9 ± 0.2	3.1 ± 0.3	1/5
3C 452 (Model I)	2746	1.19×10^{21}	1.75 ± 0.09	37 ± 2	96/89
3C 452 (Model II)	2746	1.19×10^{21}	1.5 (frozen)	23 ± 4	87/88

Note. — Spectra were fitted in the energy range 0.5 – 5.0 keV. Column 2 gives the *Chandra* background-subtracted 0.5 – 5.0 keV counts in the lobe. Column 3 gives the assumed Galactic hydrogen column density, frozen for the purposes of the fit. Errors in columns 4 and 5 are the statistical errors, 1σ for one interesting parameter. Two models were fitted to the 3C 452 data, as described in the text. Model II includes a thermal component with $kT = 0.6 \pm 0.3$ keV, consistent with the results of Isobe et al. 2002.

Table 3. X-ray flux measurements for detected lobes with insufficient counts for spectral fitting

Source	Net counts	N_{H} (cm^{-2})	$S_{1 \text{ keV}}$ (nJy)
3C 9W	13	4.11×10^{20}	0.6 ± 0.3
3C 109N	70	1.57×10^{21}	1.5 ± 0.3
3C 109S	69	1.57×10^{21}	1.5 ± 0.4
3C 173.1N	17	5.25×10^{20}	0.6 ± 0.2
3C 179E	17	4.31×10^{20}	1.3 ± 0.4
3C 179W	9	4.31×10^{20}	0.7 ± 0.3
3C 200	35	3.69×10^{20}	1.6 ± 0.4
3C 207W	23	5.40×10^{20}	0.6 ± 0.2
3C 265W	46	1.90×10^{20}	0.7 ± 0.2
3C 275.1S	20	1.89×10^{20}	0.5 ± 0.1
3C 280W	18	1.25×10^{20}	0.2 ± 0.1
3C 281N	25	2.21×10^{20}	1.0 ± 0.3
3C 334N	36	4.24×10^{20}	0.9 ± 0.3
3C 334S	36	4.24×10^{20}	0.9 ± 0.2
3C 427.1S	14	1.09×10^{21}	0.3 ± 0.1

Note. — Column 2 gives the *Chandra* background-subtracted 0.5 – 5.0 keV counts in the lobe. The 1-keV flux densities were determined by assuming a power-law with $\Gamma = 1.5$, as described in the text.

Table 4. Upper limits on the unabsorbed 1-keV flux density for the non-detected lobes.

Source	Net counts	N_{H} (cm^{-2})	$S_{1 \text{ keV}}$ (nJy)
3C 6.1N	< 14	1.75×10^{21}	< 0.4
3C 6.1S	< 15	1.75×10^{21}	< 0.5
3C 173.1S	< 17	5.25×10^{20}	< 0.6
3C 212S	< 42	4.09×10^{20}	< 1.7
3C 220.1N	< 40	1.93×10^{20}	< 1.2
3C 220.1S	< 35	1.93×10^{20}	< 1.1
3C 228N	< 12	3.18×10^{20}	< 0.8
3C 228S	< 11	3.18×10^{20}	< 0.7
3C 254W	< 16	1.75×10^{20}	< 0.4
3C 275.1N	< 11	1.89×10^{20}	< 0.3
3C 281S	< 20	2.21×10^{20}	< 0.8
3C 303E	< 23	1.60×10^{20}	< 1.0
3C 321W	< 43	4.10×10^{20}	< 0.7
3C 390.3N	< 86	3.74×10^{20}	< 1.8
3C 390.3S	< 124	3.74×10^{20}	< 2.7
3C 427.1N	< 16	1.09×10^{21}	< 0.4

Note. — Column 2 gives the 3σ upper limit of *Chandra* background-subtracted 0.5 – 5.0 keV counts. The upper limit 1-keV flux densities were determined by assuming a power-law model with $\Gamma = 1.5$, as described in the text.

In total, of the 39 lobes analysed, 23 were detected at the 3σ level or above. In Figs. 1 and 2 we show contour maps made from smoothed images for each of the sources with at least one lobe detection where the data are unpublished, or where the lobe detection has not previously been presented (3C 47, 3C 109, 3C 173.1, 3C 179, 3C 200, 3C 215, 3C 275.1, 3C 280, 3C 281, 3C 334, and 3C 427.1). Radio maps are shown in grayscale to illustrate the relation between radio and X-ray emission.

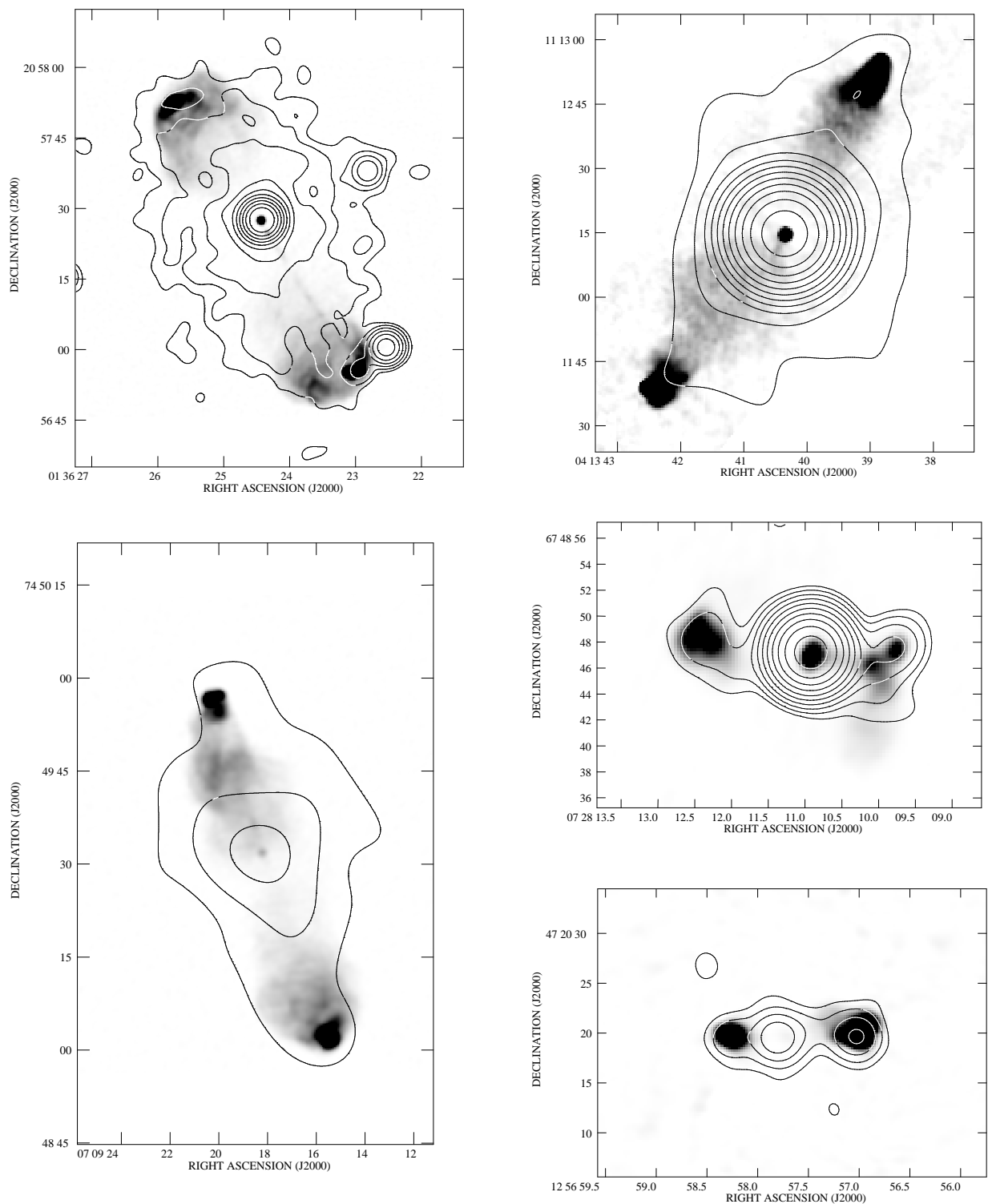


Fig. 1.— Contour maps from Gaussian smoothed 0.5 – 5.0 keV *Chandra* images of the X-ray emission from (clockwise from top left): 3C 47 ($\sigma = 1.7$ arcsec), 3C 109 ($\sigma = 4.9$ arcsec), 3C 179 ($\sigma = 1.2$ arcsec), 3C 280 ($\sigma = 1.2$ arcsec), and 3C 173.1 ($\sigma = 4.4$ arcsec). The X-ray contour levels are at 1,2,4 ... $\times 3\sigma$ level, calculated using the method of Hardcastle et al. (1998b). Radio maps shown in grayscale are from the 1.4-GHz radio maps listed in Table 5.

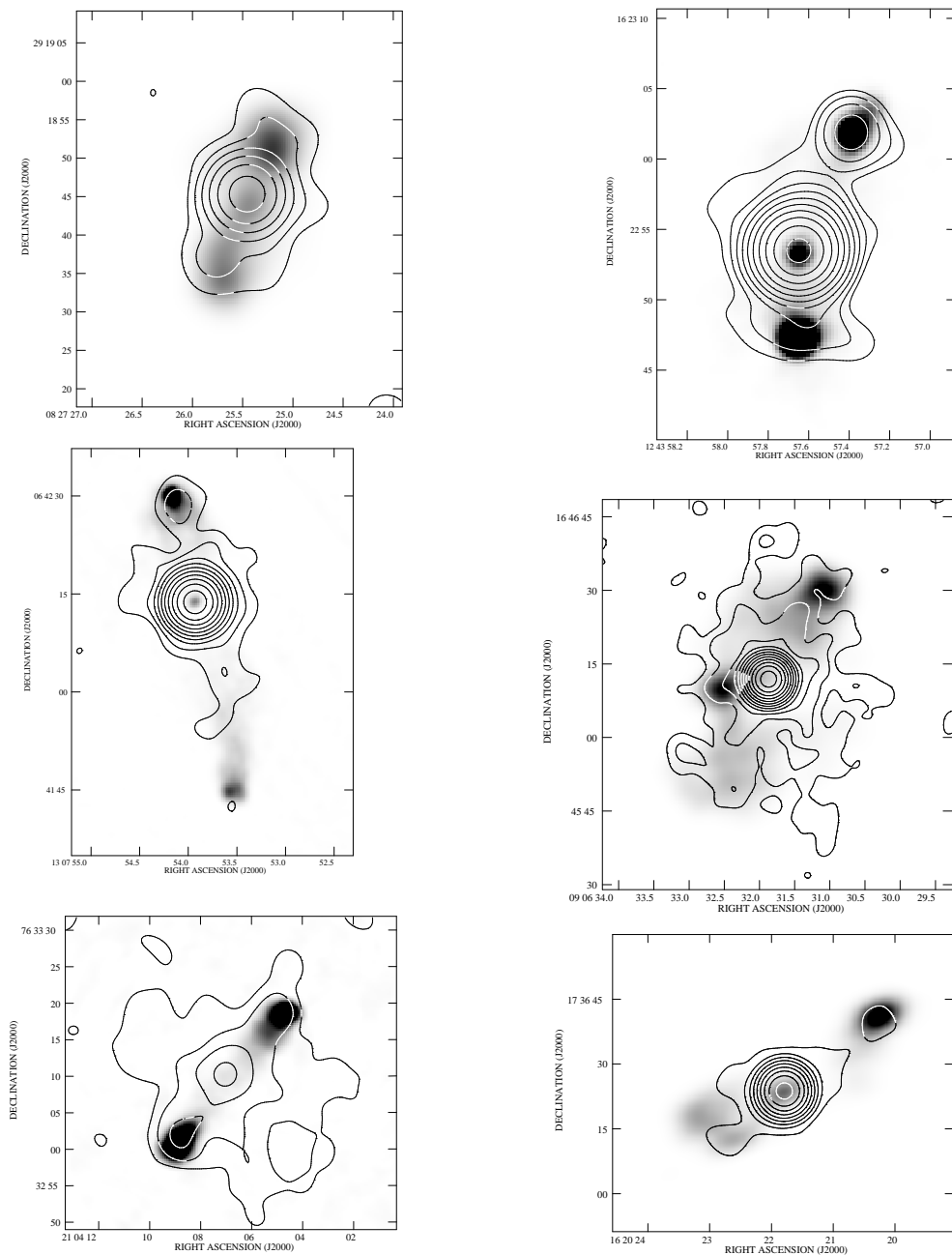


Fig. 2.— Contour maps from Gaussian smoothed 0.5 – 5.0 keV *Chandra* images of the X-ray emission from (clockwise from top left): 3C 200 ($\sigma = 2.4$ arcsec), 3C 275.1 ($\sigma = 1.2$ arcsec), 3C 215 ($\sigma = 1.7$ arcsec), 3C 334 ($\sigma = 2.4$ arcsec), 3C 427.1 ($\sigma = 1.7$ arcsec) and 3C 281 ($\sigma = 1.7$ arcsec). The X-ray contour levels are at 1,2,4 ... $\times 3\sigma$ level, calculated using the method of Hardcastle et al. (1998b). Radio maps shown in grayscale are from the 1.4-GHz radio maps listed in Table 5.

2.3. Radio data

The electrons responsible for scattering CMB photons to X-ray energies have $\Gamma \sim 1000$, and so their radio emission is emitted at $\nu \sim 100$ MHz, assuming a typical magnetic field strength of 1.5 nT ($1\text{nT} = 10\mu\text{G}$). This is at the lower end of the observable radio region. It is therefore essential to use the lowest-frequency radio maps available that have sufficient resolution to determine the extent of the radio emission and the radio spectrum of the lobes. We used the 178-MHz flux densities from the 3C and 3CRR catalogues, and obtained 1.4-GHz flux densities for each lobe using the best available maps.

For those sources where we did not have access to a 1.4-GHz radio map, we extracted archive VLA data (choosing a VLA configuration that samples the largest angular structure of each source, so as to include all of the source flux) and performed calibration and mapping using standard techniques in AIPS. Table 5 lists the radio maps used to determine the ratio of lobe flux densities and to define the X-ray spectral extraction regions.

1.4-GHz flux densities were measured using TVSTAT in AIPS. The entire extent of low-frequency radio emission was measured for each lobe, as the X-ray extraction regions were chosen using the same maps. The flux from any hotspots or jets was excluded. 178-MHz flux densities for each lobe were then estimated by scaling the 3C or 3CRR flux densities based on the ratio between the 1.4-GHz flux densities for that lobe and the total 1.4-GHz flux densities from the lobes. Here we assume that the 178-MHz flux density is dominated by emission from the radio lobes, so that jet and hotspot emission is not important at that frequency. This procedure also implicitly assumes that the low-frequency spectral indices are the same for both lobes of a given source. In general this assumption has not been tested, but since we know the high-frequency spectral indices of the lobes in a given source are rarely very different (Liu and Pooley 1991), it seems unlikely that it is seriously wrong. We have verified that low-frequency lobe spectral indices are similar where suitable data (e.g., 330-MHz radio maps) are available to us: the results of this investigation suggest that the inferred 178-MHz lobe flux densities are likely to be wrong by at most 20%, which would correspond to a systematic error in the predicted inverse-Compton emission of around 10%.

Table 5. Radio maps used in the analysis

Source	Frequency (GHz)	Date observed	Reference/Proposal ID
3C 6.1	1.48	1987 Oct 03	AH291
3C 9	1.54	1992 Dec 13	AL280
3C 47	1.65		1
3C 109	1.45		2
3C 173.1	1.48		3
3C 179	1.65	1986 Mar 21	AC150
3C 200	1.49	1987 Nov 15	AH271
3C 207	1.54	1992 Dec 13	AL280
3C 212	1.66	1982 Mar 01	LAIN
3C 215	1.49	1987 Nov 15	AH271
3C 219	1.52		4
3C 220.1	1.40	1995 Oct 00	AH568
3C 228	1.42	1986 Jul 12	AL113
3C 254	1.56	1989 Feb 01	AB522
3C 265	1.42	1986 Jul 12	AL113
3C 275.1	1.49	1989 Jan 21	AP158
3C 280	1.56	1989 Feb 01	AB522
3C 281	1.43	1992 Nov 18	AB631
3C 303	1.45		3
3C 321	1.51	1986 Dec 02	AV127
3C 334	1.49	1986 Jul 12	AL113
3C 390.3	1.45		5
3C 427.1	1.54	1986 Jun 04	AL113
3C 452	1.41		1

Note. — Observation dates are given for the archive data. References are given for published maps (where the electronic image was obtained from the 3CRR database, Leahy et al. 1998), and VLA proposal IDs for

archive data.

References. — (1) Leahy et al. 1998; (2) Giovannini et al. 1994; (3) Leahy and Perley 1991; (4) Clarke et al. 1992; (5) Leahy and Perley 1995.

3. Synchrotron and inverse-Compton modelling

We used the X-ray flux densities or upper limits given in Tables 2, 3 and 4, and radio flux densities at 178 MHz and 1.4 GHz obtained as described in Section 2.3, to carry out synchrotron and inverse-Compton modelling using SYNCH (Hardcastle et al. 1998a) for the sources not previously analysed using this method. The radio lobes were modelled either as spheres, cylinders or prolate ellipsoids, depending on the morphology of the low-frequency radio emission. As the angle to the line of sight is not well constrained for most of the sources, the source dimensions are the *projected* dimensions. This is not a good approximation, as sources in the sample will lie at all angles to the line of sight. We discuss the likely effects of this approximation later.

In each case we used the radio flux densities to normalize the synchrotron spectrum. We initially assumed a broken power-law electron distribution with initial electron energy index, δ , of 2, $\gamma_{\min} = 10$ and $\gamma_{\max} = 10^5$, and a break energy in the range $\gamma_{\text{break}} = 1200 - 10000$, chosen so as to fit the two radio data points. In many cases the assumed spectral break (of 1 in electron energy index) was not sufficiently large to fit the radio data. In these cases we instead lowered γ_{\max} to fit the high-frequency slope of the radio spectrum. The effective γ_{\max} is expected to decrease as the synchrotron plasma ages and/or expands, so this is a physically plausible change to make. The choice of γ_{\max} does not significantly affect the prediction for CMB IC, as electrons with $\gamma \ll \gamma_{\max}$ are responsible for the scattering to X-ray energies. (The prediction for SSC emission is significantly reduced if γ_{\max} is reduced; however, SSC is not the dominant emission process in any of the sources.) The choice of parameters that affect the low-energy electron population (δ and γ_{\min}) has a more important effect on the predicted inverse-Compton flux. We therefore discuss the effect of modifying these parameters on our results and justify our adopted values in more detail in Section 5.2. In Table 6, we give the parameters of the synchrotron model for each radio lobe.

We then determined the predictions for CMB IC and SSC at 1 keV based on the modelled synchrotron spectrum for each source, assuming equipartition between radiating particles and magnetic field and a filling factor of unity. For 3C 452, we adopted the 1-keV flux density from the two-component fit, which gave a better fit statistic than the single power-law model. Table 7 gives the observed and predicted fluxes for each source in the sample, including the previously published sources.

Table 6. Synchrotron model parameters and radio spectral information for each source.

Source	γ_{\max}	γ_{break}	Shape	r (arcsec)	S_{178} (Jy)	$S_{1.4}$ (Jy)
3C 6.1N	3000		C	4.96	9.7	0.37
3C 6.1S	3000		C	4.22	5.2	0.2
3C 9W	3000		S	2.7	14.6	0.67
3C 47N	6000		S	15	13.1	0.69
3C 47S	6000		S	17.96	15.7	0.83
3C 109N	4000		E	13	11.0	0.86
3C 109S	5000		E	13.6	12.5	0.98
3C 173.1N	5000		E	8.34	9.4	0.83
3C 173.1S	6000		S	10.5	7.4	0.66
3C 179E	100000	3000	S	5.29	6.7	0.94
3C 179W	100000	3000	S	3.81	2.6	0.37
3C 200	100000	2000	S	13.3	12.3	1.52
3C 207W	3000		S	4.32	5.9	0.24
3C 212S	4000		S	3	0.07 ^a	0.65
3C 215N	5000		S	13.5	7.3	0.41
3C 215S	6000		E	13.4	5.1	0.29
3C 219N	100000	4000	C	45.3	23.3	2.9
3C 219S	100000	3400	C	34.5	21.6	2.7
3C 220.1E	100000	1200	S	11.1	8.0	0.86
3C 220.1W	100000	1200	S	9.7	9.2	1.0
3C 228N	100000	2000	C	7.02	9.6	1.3
3C 228S	100000	2000	C	7.36	14.2	1.9
3C 254W	2600		S	4.7	13.9	0.16
3C 265E	4000		C	9.3	11.9	0.33
3C 265W	5000		C	7.9	9.4	0.26
3C 275.1N	2800		S	6.1	8.2	0.16
3C 275.1S	2800		S	5.35	11.7	0.23
3C 280W	2000		S	3.8	14.9	0.11
3C 281N	100000	1800	S	8.86	2.9	0.31
3C 281S	100000	1800	C	9.68	3.11	0.34

Table 6—Continued

Source	γ_{\max}	γ_{break}	Shape	r (arcsec)	S_{178} (Jy)	$S_{1.4}$ (Jy)
3C 303E	3000		S	9.3	12.2	0.39
3C 321W	5000		S	33.1	7.6	0.09
3C 334N	100000	2000	S	10.6	6.9	0.80
3C 334S	1000	1800	S	7.88	5.0	0.50
3C 390.3N	6000		S	39	21.6	1.65
3C 390.3S	6000		S	48.3	30.2	2.3
3C 427.1N	100000	2000	C	4.85	12.8	1.7
3C 427.1S	100000	2000	C	4.59	16.2	2.1
3C 452	100000	6000	C	88.96	59.3	10.5

Note. — Shapes are S: sphere, C: cylinder and E: ellipsoid. r is the equivalent spherical radius of the modelled volume. S_{178} and $S_{1.4}$ are the assumed 178-MHz radio flux density and the measured 1.4-GHz flux density, respectively. γ_{\min} is 10 in all cases.

^aFor this source it was not possible to use a 178-MHz flux density, because it was impossible to determine the flux ratio of the two lobes from the 1.4-GHz map (of very low resolution). We therefore used the 8-GHz flux density (given here) to constrain the spectrum instead.

Table 7. Observed and predicted X-ray flux densities at 1 keV for the IC models.

Source	1-keV flux densities (nJy)				R
	Observed	Predicted SSC	Predicted CMB-IC	Total predicted	
3C 6.1N	< 0.4	–	0.5	0.5	< 0.8
3C 6.1S	< 0.5	–	0.3	0.3	< 1.7
3C 9W	0.6	–	0.7	0.7	0.9 ± 0.4
3C 47N	3.6	–	1.1	1.1	3.3 ± 0.6
3C 47S	10	–	1.6	1.6	6.3 ± 0.6
3C 109N	1.5	–	0.7	0.7	2.1 ± 0.4
3C 109S	1.5	–	0.8	0.8	1.9 ± 0.5
3C 173.1N	0.6	–	0.3	0.3	2.0 ± 0.7
3C 173.1S	< 0.6	–	0.4	0.4	< 1.5
3C 179E	1.3	0.04	0.4	0.4	3.3 ± 1
3C 179W	0.7	0.01	0.14	0.15	4.7 ± 2
3C 184N	0.2	0.103	0.051	0.154	1.3 ± 0.7
3C 200	1.6	0.02	1.2	1.2	1.3 ± 0.3
3C 207W	0.6	–	0.2	0.2	3 ± 1
3C 212S	< 1.7	0.006	0.05	0.06	< 28
3C 215N	2.9	–	0.7	0.7	4.1 ± 0.6
3C 215S	2.9	–	0.6	0.6	4.8 ± 0.8
3C 219N	9	0.02	3.3	3.3	2.7 ± 0.3
3C 219S	7	0.02	2.2	2.2	3.2 ± 0.2
3C 220.1E	< 1.2	0.01	1.0	1.0	< 1.2
3C 220.1W	< 1.1	0.02	0.9	0.9	< 1.2
3C 223N	3.1	0.004	1.3	1.4	2.2 ± 0.4
3C 223S	3.0	0.004	1.2	1.2	2.5 ± 0.4
3C 228N	< 0.8	0.02	0.5	0.5	< 1.6
3C 228S	< 0.7	0.04	0.6	0.6	< 1.2
3C 254W	< 0.4	–	0.5	0.5	< 0.8
3C 263NW	0.8	0.004	0.2	0.2	4.0 ± 1.0
3C 263SE	0.5	0.001	0.1	0.1	5.0 ± 2.0
3C 265E	3.1	–	1.2	1.2	2.6 ± 0.3
3C 265W	0.7	–	0.8	0.8	0.9 ± 0.2

Table 7—Continued

Source	1-keV flux densities (nJy)				R
	Observed	Predicted SSC	Predicted CMB-IC	Total predicted	
3C 275.1N	< 0.3	–	0.4	0.4	< 0.8
3C 275.1S	0.5	–	0.4	0.4	1.3 ± 0.3
3C 280W	0.2	–	0.6	0.6	0.3 ± 0.2
3C 281N	1.0	0.003	0.4	0.4	2.5 ± 0.8
3C 281S	< 0.8	0.003	0.5	0.5	< 1.6
3C 284E	1.9	0.003	0.93	0.94	2.0 ± 0.2
3C 284W	0.90	0.002	0.82	0.82	1.1 ± 0.2
3C 292	4.1	0.01	2.42	2.43	1.7
3C 303E	< 1.0	–	0.3	0.3	< 3.3
3C 321W	< 0.7	–	1.0	1.0	< 0.7
3C 322	1.4	0.05	1.3	1.4	1.0
3C 330NE	0.28	0.01	0.12	0.13	2.2 ± 0.8
3C 330SW	0.32	0.01	0.13	0.14	2.3 ± 0.6
3C 334N	0.9	0.01	0.7	0.7	1.3 ± 0.3
3C 334S	0.9	0.007	0.40	0.40	2.3 ± 0.5
3C 351N	1.1	0.001	0.15	0.15	7.3 ± 2.0
3C 351S	0.7	0.001	0.12	0.12	5.8 ± 2.5
3C 390.3N	< 1.8	–	1.4	1.4	< 1.3
3C 390.3S	< 2.7	–	2.3	2.3	< 1.2
3C 403E	1.63	0.002	0.35	0.35	4.6 ± 2.1
3C 403W	1.38	0.002	0.34	0.34	4.0 ± 2.1
3C 427.1N	< 0.4	0.05	0.3	0.4	< 1.0
3C 427.1S	0.3	0.08	0.3	0.4	0.8 ± 0.3
3C 452	23	0.4	7.8	7.8	2.9 ± 0.5

Note. — Flux densities are predicted from the radio data on the assumption of equipartition using the SYNCH code as described in the text. Where no SSC flux density is quoted, the predicted value was less than 1 pJy, and so is irrelevant to the total inverse-Compton

flux density. R is the ratio of observed to predicted total 1-keV flux density. Errors on the R value are entirely due to the uncertainties on the 1-keV flux densities, as quoted in this paper or the papers in which they were originally measured, and do not take into account any systematic uncertainties. For the sources where the spectral modelling details are not given in Table 6, the results are taken from the paper referred to in Table 1.

4. Results

To study the overall properties of the sample, we first constructed a histogram of R , the ratio of observed to predicted X-ray flux at equipartition. Fig. 3 shows histograms of R for the detected and non-detected lobes. Note that $R = 1$ means that the CMB plus SSC model with an equipartition magnetic field and filling factor of unity can explain the observed X-ray flux. For $R > 1$, in an IC model, either the magnetic field is lower than the equipartition value, i.e., the lobes are electron dominated, or an additional photon field is present; $R < 1$ implies magnetic domination. We neglect here the effects of a filling factor less than one, which could be the case either for electrons, magnetic field or both. If the electrons fill only a fraction of the lobe volume with a uniform field, we will *underestimate* R , since the predicted CMB IC flux depends on the number density of electrons, which we will have overestimated. If there are strong magnetic field variations, but a uniform electron density, we will *overestimate* R , because our prediction for the number density and therefore CMB IC flux will be an underestimation. The effect of filling factor is discussed in more detail in Hardcastle and Worrall (2000).

Table 8 gives the measured and equipartition magnetic field strengths or upper limits and their ratio. We also list the ratio of electron to magnetic field energy densities, for comparison with other work in the literature. However, the electron and magnetic field energies are sensitive to small changes in magnetic field strength, so that the uncertainty on the value of U_e/U_b is large. We therefore consider R and B_{obs}/B_{eq} to be better measures of the departure from equipartition. For comparison with other results in the literature, we note that R relates to the two other commonly used measures of the departure from equipartition as $(B_{obs}/B_{eq}) \propto R^{\frac{-2}{\delta+1}}$ and $(U_e/U_b) \propto R^{\frac{\delta+5}{\delta+1}}$, where δ is the electron energy index ($2 \leq \delta \leq 3$).

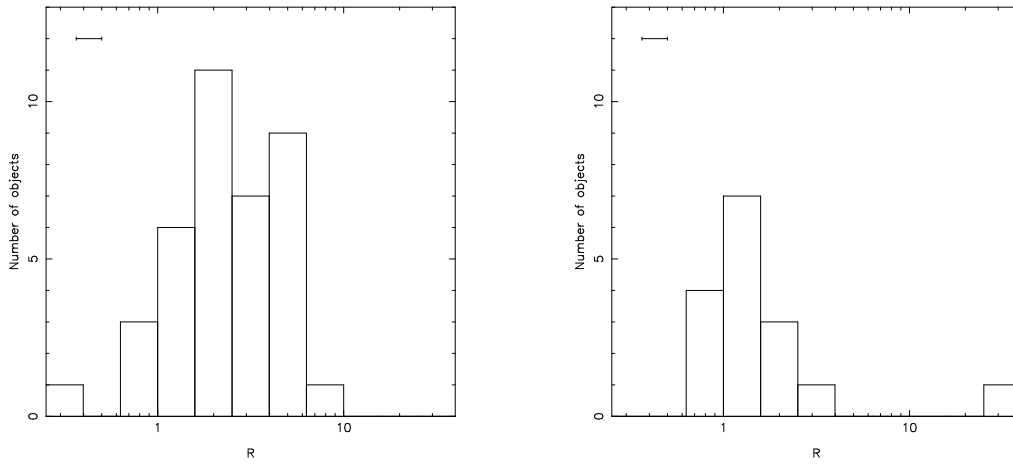


Fig. 3.— Distribution of R values for the lobe sample. The left-hand plot shows the detected lobes and the right-hand plot shows the upper limits for non-detected lobes. A representative error bar is shown in the top left-hand corner of the left-hand plot.

The distribution of R values for the detected sources is quite narrow, with the most extreme values being 0.3 and 7.3 (U_e/U_b ranges from 0.2 to 53). The majority of the sources have $R > 1$, and appear to be distributed around a peak at $R \sim 2$. However, the upper limits, in addition to the one detected source with $R < 1$, show that some FR II radio lobes could be magnetically dominated by at least a factor of 2 (or have a strongly structured magnetic field). Since the non-detections are only a small fraction of the sample, we can conclude that $> 36/54$ lobes, or ~ 70 percent of FR II radio galaxies and quasars if our sample is representative, are either at equipartition or electron dominated.

We next examined whether the type of radio source affects the observed R value, by comparing the distributions of R for narrow-line radio galaxies and for broad-line objects (broad-line radio galaxies and radio-loud quasars). In the widely accepted unification model for radio galaxies and radio-loud quasars (e.g., Barthel 1989; Urry and Padovani 1995), these two categories of source, which possess different optical properties but similar radio structure, are thought to be the same objects seen at different angles to the line of sight. The narrow-line objects are thought to occupy angles between 45° and the plane of the sky, whereas the radio-loud quasars and broad-line radio galaxies occupy angles between 45° and the line of sight, with the difference in optical properties resulting from the presence of a torus of cold material along our line of sight to the narrow-line objects, which obscures the AGN in those sources. We excluded the (few) low-excitation objects (Laing et al. 1994) from our comparison to avoid confusion. Fig. 4 shows a histogram with the two categories of source indicated (only detected lobes are included; however, the fraction of non-detections in the two subsamples are similar). It is immediately apparent that the distributions of R differ, in the sense that broad-line objects typically have higher values of R . The broad-line objects nearly all have $R > 2$, whereas the narrow-line objects mainly have $R < 2$. The median values of the samples are 2.1 (narrow-line) and 3.1 (broad-line). A median test rejects the hypothesis that the two subsamples have the same median with ~ 92 percent probability.

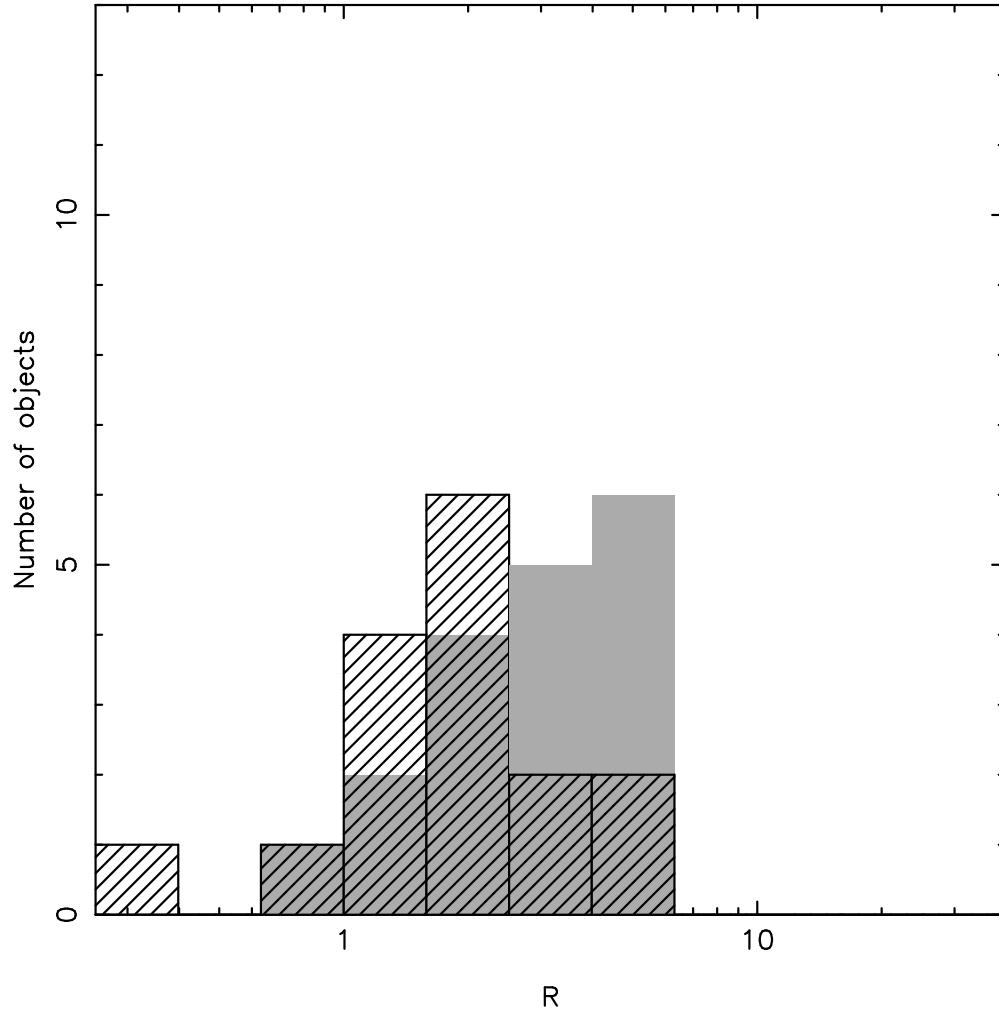


Fig. 4.— The R distribution for the narrow-line and broad-line objects. The distribution for broad-line radio galaxies and quasars is indicated with filled rectangles, and that for narrow-line radio galaxies is overlotted in hatched rectangles.

One likely explanation for this marginally significant difference is the effect of projection on the volumes of the lobes. The predicted X-ray flux from CMB IC is proportional to the product of lobe volume and electron density. The electron density scales as $V^{-4/7}$ (Hardcastle et al. 2004), so that the predicted X-ray flux $S_{cmb} \propto V^{3/7}$. Since we have not taken projection effects into account, this means that for most sources we have underestimated the source volume and therefore S_{cmb} , so that R for a given source will be likely to be overestimated. The effect will be at its most severe for the broad-line radio galaxies and quasars, thought to be within 45 degrees of the line-of-sight, where the volumes will have been significantly underestimated. If we assume that the population of narrow-line radio galaxies occupies all angles between 45° and the plane of the sky with equal probability, then the most probable angle at which to observe a narrow-line radio galaxy is at ~ 70 degrees, where R will be overestimated by a factor of ~ 1.06 , assuming that volume scales as l , where l is the observed lobe length. Similarly, assuming that the population of broad-line radio galaxies and quasars occupies all angles between 45° and the line of sight with equal probability, then the most probable angle at which to observe a broad-line radio galaxy or quasar is at ~ 30 degrees, where R will be overestimated by a factor of ~ 1.34 . (Note that for angles less than 5 – 10 degrees, R can be overestimated by a factor of > 2). These results show that the difference in the medians of the two samples cannot entirely be explained by a model in which the intrinsic value of R is the same for all radio galaxies and quasars.

To investigate this further, we carried out Monte Carlo simulations to examine whether a narrow distribution of intrinsic R values could produce the observed distribution in R as a result of projection effects. We simulated samples of 10^6 radio galaxies and quasars, distributed at angles to the line of sight with a probability distribution $P(\theta)d\theta = \sin(\theta)d\theta$ (i.e., based on the assumption that the lobes are randomly oriented with respect to the plane of the sky), and having an intrinsic Gaussian distribution of R with a mean $\langle R \rangle$ and variance σ . We then determined the *observed* R for each simulated source, taking into account projection [$R_{app} \propto (\sin(\theta))^{-3/7}$], assuming cylindrical lobes (with $V \propto l$). We compared the simulated distribution of R_{app} to the observed distribution using a K-S test, and found that the intrinsic values for $\langle R \rangle$ and σ that give the best match to the observed data are 2.5 and 1.15, respectively. We next tested whether the observed distributions of R for the narrow-line and broad-line objects could separately be explained by this intrinsic distribution. We find that the broad-line objects have a ~ 40 percent probability of being drawn from a parent population having this intrinsic distribution; however, the narrow-line objects have only a ~ 3 percent chance of being drawn from such a population. The intrinsic distribution that gives the best fit to the narrow-line objects alone has $\langle R \rangle = 1.7$ and $\sigma = 1.25$ (observed R for the narrow-line and broad-line subsamples are 2.1 ± 1.1 and 3.2 ± 1.0 , respectively).

We therefore conclude that projection is likely to be important in explaining the distribution of observed R values; however, some additional explanation may be needed to explain the differences between the narrow-line and broad-line objects. We note, however, that the *actual* distribution of inclination angles in this sample is unknown; it is clear from the fact that it contains roughly equal numbers of narrow and broad-line objects that the probability distribution of line-of-sight angle we used for the simulation does not accurately represent the actual distribution in our sample. It is also possible that the high redshift quasars (which often have high R values) may be biased towards small angles to the line of sight, since the radio flux observed at 178-MHz in the highest redshift objects may have contributions from beamed components (although this will also reduce the intrinsic radio flux, which will act in the opposite direction to raise the observed value of R). Another possibility is that the systematic uncertainties in the X-ray analysis may be worse for the quasars, as contamination from the bright central source will be harder to remove; this could be compounded by the fact that the quasars are typically more distant and so have smaller angular sizes (although we find no correlation between R and angular size).

Table 8. Magnetic field strengths and contributions to energy density.

Source	B_{eq} (nT)	B_{obs} (nT)	$B_{\text{obs}}/B_{\text{eq}}$	U_e/U_B
3C 6.1N	3.5	> 3.5	> 1.0	< 1
3C 6.1S	3.4	> 2.5	> 0.74	< 3
3C 9W	10.0	11.0	1.1	0.70
3C 47N	1.2	0.6	0.5	15
3C 47S	1.1	0.4	0.36	53
3C 109N	1.3	0.85	0.71	5
3C 109S	1.3	0.85	0.71	5
3C 173.1N	1.8	1.2	0.67	4
3C 173.1S	1.3	> 1.0	> 0.77	< 3
3C 179E	2.9	1.3	0.45	< 19
3C 179W	2.9	1.1	0.38	37
3C 200	1.4	1.1	0.79	3
3C 207W	3.2	2.0	0.63	6
3C 212S	7.4	> 1.0	> 0.14	< 177
3C 215N	1.2	0.6	0.5	13
3C 215S	1.0	0.45	0.45	25
3C 219N	0.6	0.35	0.58	6
3C 219S	0.7	0.4	0.57	8
3C 220.1E	1.7	> 1.7	> 1	< 1
3C 220.1W	1.9	> 1.9	> 1	< 1
3C 223N	0.35	0.22	0.63	5
3C 223S	0.37	0.20	0.54	9
3C 228N	2.3	> 1.8	> 0.78	< 2
3C 228S	2.4	> 2.4	> 1	< 1
3C 254W	3.9	> 3.9	> 1.0	< 1
3C 265E	2.1	1.3	0.62	7
3C 265W	2.3	2.3	1.0	1
3C 275.1N	2.5	> 2.8	> 1.1	< 0.7
3C 275.1S	3.1	2.8	0.9	1
3C 280	5.5	9.0	1.6	0.2
3C 281N	1.4	0.9	0.64	6

Table 8—Continued

Source	B_{eq} (nT)	B_{obs} (nT)	$B_{\text{obs}}/B_{\text{eq}}$	U_e/U_B
3C 281S	1.4	> 1.0	> 0.71	< 3
3C 284E	0.52	0.40	0.76	3
3C 284W	0.48	0.48	1.0	1
3C 303E	1.9	> 0.9	> 0.47	< 15
3C 321W	0.60	> 0.7	> 1.2	< 0.6
3C 334N	1.5	1.5	1	1
3C 334S	1.8	1.1	0.61	6
3C 390.3N	0.7	> 0.7	> 1	< 1
3C 390.3S	0.7	> 0.7	> 1	< 1
3C 403N	0.5	0.2	0.40	27
3C 403S	0.5	0.2	0.40	23
3C 427.1N	3.3	> 3.3	> 1	< 1
3C 427.1S	3.7	3.7	1	1
3C 452	0.5	0.25	0.50	9

Note. — Column 2 is the equipartition magnetic field strength, column 3 is the magnetic field strength inferred from the level of X-ray flux, column 4, the ratio of observed to equipartition field strength, and column 5 the ratio of electron energy density to magnetic field energy density. Note that $1\text{nT} = 10\mu\text{G}$.

Hardcastle et al. (2004) carried out a similar analysis to that presented here for the X-ray properties of hotspots in FR II radio sources. They found that hotspots exhibit a large range in R values, up to $R \sim 1000$, and conclude that a second X-ray emission component due to synchrotron radiation must be present in some hotspots. In this analysis we find that the IC model can explain all X-ray lobe detections, with magnetic field strengths ranging from a fifth of the equipartition value to slightly higher than the equipartition value. This is unsurprising, as there is no known efficient acceleration mechanism in the lobes that can produce electrons of X-ray-synchrotron-emitting energies, whereas electrons at the hotspots could be shock-accelerated to the energies required for X-ray emission. Hardcastle et al. also find that R is correlated with radio luminosity, so that the highest R values are found in the weakest radio sources; they interpret this as being caused by a luminosity-dependent cutoff in the maximum energy to which the electrons are accelerated at the hotspot. We find no correlation between R and radio luminosity for the radio lobe sample. There is also no correlation between R and redshift. Finally, there is no correlation between the lobe R values and the hotspot R values for the same sources taken from Hardcastle et al., as expected, since we believe that the X-ray emission mechanisms in lobes and hotspots are different.

As part of a study of X-ray emission from jets, hotspots and lobes, Kataoka and Stawarz (2005) investigated the X-ray emission processes in a sample of 18 previously detected radio lobes. They conclude that inverse-Compton emission with an equipartition magnetic field is the best model for lobe X-ray emission for their smaller sample, in good agreement with our results. Together with the work we present here, these results provide strong support for the argument that FR II radio lobes are near to equipartition.

To summarize, we find that detectable X-ray emission from the lobes of FR II radio galaxies and quasars is common, that it is due predominantly to IC scattering of CMB photons, and that most FR II sources are close to equipartition, with the energy densities perhaps being electron-dominated by a factor of a few. In the next sections, we discuss reliability issues, and alternative explanations of our results.

5. Discussion

5.1. Reliability issues

As discussed in Appendix A, our conclusions in several cases differ significantly from the work of previous authors. It is extremely difficult to obtain a correct flux measurement for lobe-related X-ray emission, because the best choice of extraction regions is sometimes uncertain. It is difficult to avoid AGN contamination, particularly when the radio-lobe

emission lies close to the core, and it is also important to exclude any contribution from a hot-gas atmosphere. We have carefully chosen our background regions to be at the same distance from the nucleus as the source regions, although in two cases (3C 200 and 3C 452) this was not possible because the radio-related X-ray emission surrounds the core. We believe that it is the difficulty of correctly separating the different components of the X-ray emission that has led to discrepant results in the literature. It is extremely unlikely that any of our flux measurements are *under*-estimates of the lobe IC emission, so that any systematic uncertainty in the R values is likely to be in the direction of overestimation. As mentioned in Section 4, overestimation of R values may be a particular problem for some of the quasars with strong AGN and small angular sizes.

5.2. Assumptions about the low-energy electron population

As mentioned in Section 1, the properties of the low-energy electron population in the radio lobes are not well constrained, largely due to the lack of instruments capable of measuring the synchrotron emission from this population. This is particularly problematic when studying the IC/CMB process, as it is the low-energy electrons that scatter the CMB to X-ray energies. Since we cannot use observations to constrain directly the electron energy distribution below 178 MHz for our sample, it is necessary to assume a low-frequency spectral index, δ , and cutoff energy, γ_{\min} . For this work, we assumed that at low energies, the electron population has an energy index $\delta = 2$, which corresponds to the prediction from shock acceleration. This prediction is supported by observations of hotspots (e.g., Meisenheimer et al. 1997), which have the low-frequency spectral index predicted by the models. We therefore assume that the electron population in the lobes has been shock-accelerated while passing through the hotspots, resulting in an initial energy distribution with $\delta = 2$ (corresponding to a spectral index $\alpha = 0.5$). Spectral ageing has then steepened the spectrum at observable frequencies to the observed values of 0.5 – 1.0. Our modelled energy distribution (Section 3) is therefore a power-law of index 2 at low energies, with a break to a steeper slope in the observable radio region. We also chose to use $\gamma_{\min} = 10$, motivated partly by observations of $\gamma_{\min} \sim 100 - 1000$ in hotspots (e.g., Carilli et al. 1991) – we would expect a lower γ_{\min} in lobes due to the effects of adiabatic expansion – and partly to be conservative. We believe that, given the lack of knowledge about this electron population, our chosen electron energy distribution is physically plausible; however, it is important to consider the effects of varying δ and γ_{\min} , particularly since the measured X-ray spectral index for those sources where a spectral model could be fitted is steeper than 0.5 in a few cases.

We first tested the effects of varying γ_{\min} for several of our sources, covering a range of R

values. If we adopt $\gamma_{\min} = 1000$, corresponding to the lower limit of observed radio emission from lobes, we find new R values that do not differ from the quoted values (Table 7) for $\gamma_{\min} = 10$ within the 1σ errors. The reason that the prediction for X-ray inverse-Compton emission does not change significantly is that, while the reduced energy range decreases the electron density, the normalization of the electron energy spectrum increases in order to maintain equipartition.

We next tested the effect of varying δ . An alternative approach to our method is to assume that the electron energy index implied by the low-frequency radio spectral index can be extrapolated back to γ_{\min} . We tested the effect of this assumption, using the 3CRR spectral index α measured between 178 MHz and 750 MHz (tabulated in Table 1), which are always greater than 0.5, for several of our sources, using $\gamma_{\min} = 10$ and assuming $\delta = 1 + 2\alpha$ and including a break or high-energy cutoff in the spectrum as needed to fit to the radio spectrum, as in our main analysis. We found that for all of the sources this resulted in a *lower* prediction for the X-ray inverse-Compton flux, increasing the R values by a factor of ~ 2 . The reason for the lower IC prediction in this case is that the equipartition requirement causes the electron energy spectrum normalization to be lowered with respect to the $\delta = 2$ calculation because of the large contribution to the electron energy density made by the additional low-energy electrons. If we adopt $\gamma_{\min} = 1000$ for this analysis, the electron normalization increases again, because of the reduced energy range, so that the resulting R values are again roughly consistent with those in Table 7. We therefore conclude that uncertainty in the distribution of electrons at low energies introduces at most a factor of 2 uncertainty into our quoted R values. This corresponds to a factor of 0.7 in B_{obs}/B_{eq} and 4 in U_e/U_b .

5.3. Anisotropic inverse-Compton emission from a nuclear photon field

Our analysis for 3C 265 in Section A.5 and for 3C 284 (Croston et al. 2004), as well as the analysis of Belsole et al. (2004) for 3C 184, shows that IC scattering of the photon field from a hidden quasar does not appear to be the dominant X-ray emission mechanism in these sources. As mentioned in Section A.5, the X-ray emission from the IC/nuclear process would be brightest towards the nucleus and decrease rapidly with radius; this is not the morphology that is observed. In contrast, the X-ray emission from CMB IC is expected to follow closely the structure of the low-frequency radio emission, which appears to be the case for those sources where the signal-to-noise is sufficiently high to observe the spatial distribution of emission. Our calculations for IC/nuclear (Section A.5), in contrast to the work of other authors, assume that the incident photon field is emitting isotropically. The justification

for this assumption comes from observations of the infrared emission from narrow-line and broad-line objects which show that the infrared properties of the two types of object are the same (Meisenheimer et al. 2001). IC/nuclear emission may be important in some sources in this sample, and may help explain the different distributions of narrow-line and broad-line objects. 3C 207 (Brunetti et al. 2002) may be an example where this process is important. However, we have shown that CMB IC with a near equipartition magnetic field can account for the majority of the observed X-ray emission in most narrow-line radio galaxies (and, if projection is taken into account, in many broad-line and objects as well); we conclude that in most cases IC/nuclear is not the dominant process.

5.4. An alternative interpretation: shock-heated gas?

As discussed in the context of our observations of 3C 223 and 3C 284 (Croston et al. 2004), it is also possible that there is hot, shocked gas surrounding the radio lobes of some sources. The emission from such gas could be mistaken for IC emission, as it is difficult to distinguish spectrally between these models due to the small number of counts from most of the lobes. However, in the cases where spectral fitting could be performed, a thermal model was usually a significantly poorer fit to the data. As mentioned above, the lack of a correlation between R and redshift also suggests that the emission is not dominated by such shocked gas, which would be difficult to detect at high redshifts (based on the assumption that most FRIIs reside in groups, as found by Best (2004), and assuming a typical group luminosity of 10^{42} erg s $^{-1}$). In addition, many of the sources have radio morphologies similar to 3C 223 and 3C 284 (Croston et al. 2004), for which we argue that highly supersonic expansion is unlikely. These arguments do not rule out some contribution from hot gas. However, the results from 3C 452, where a two-component model could be fitted, show that it is not possible to explain all of the excess X-ray emission above the equipartition prediction by contamination from thermal emission.

As an additional test, we can compare the expected luminosity of shock-heated gas with the observed luminosity in sources where some estimate of the physical conditions in the external medium has been made. We assume a shock-heated shell surrounding the entire lobe. The temperature of the shock-heated gas is unknown, though the evidence from spectral fits, where these are possible, is that it must be high ($\gtrsim 5$ keV). Fortunately *Chandra's* response to gas hotter than a few keV is only weakly sensitive to temperature, so this does not restrict our ability to carry out these calculations. We make the assumption that the shock-heated material is gas swept up in the radio lobe's expansion, compressed by some compression factor k : then if the number of particles swept up by the lobe is N ,

and the lobe’s volume is V , the mean density of particles in the shell is kN/V . Assuming uniform density, the luminosity from the shocked shell is CN^2k/V , where C is a constant (depending on the luminosity band of interest, the metal abundance of the shocked material, and, weakly, on its temperature). The compression factor is unknown, but given the close match of the detected X-rays to the shape of the radio-emitting lobes, must be significantly greater than 1: application of standard jump conditions would give $k = 4$, while the observed shock around the southern lobe of Cen A (Kraft et al. 2003) corresponds to $k \approx 10$. We have calculated the expected luminosity for shocked shells in several sources for which we have estimates of the group/cluster parameters (e.g., Hardcastle et al. 2002; Croston et al. 2004). In general we find that the expected luminosity for $k > 1$ exceeds the observed luminosity of the lobes; what we observe is too faint to be compressed, swept-up gas. (The exceptions to this rule are sources that are found to lie in reasonably rich environments: for example, $k = 4$ is allowed by the data for 3C 263.) While the results are uncertain because the physical parameters of the environments are poorly constrained, we consider the general incompatibility of this simple model with the observations to be an additional argument against the picture in which the lobe-related X-rays are due to shock-heated thermal material. If supersonic expansion occurred in a small region of the lobe, e.g., around a hotspot, then the expected luminosity from the shocked gas would be lower, and could be compatible with the observations. However, in the largest sources with high signal-to-noise detections (e.g., 3C 452), the X-ray emission is not localized in this way, and any emission from shock-heated gas close to hotspots will have been excluded from our analysis. We therefore conclude that this scenario is probably unimportant for the majority of sources in the sample, although it could contribute in some high R sources where the data quality is insufficient to rule out localized shock heating.

5.5. Implications for particle content

If the lobes of FR II sources contained an energetically dominant population of relativistic protons (with a high ratio of U_p/U_e), and the energy densities in magnetic field and *particles* were similar, then R would be expected to be typically less than unity. Our results therefore rule out a model where FR II radio lobes have an energetically important proton population and are at equipartition. It is not possible to rule out directly a model in which radio lobes are highly particle-dominated, i.e., where there is an energetically important population of protons giving a total energy density in particles that is an order of magnitude or more higher than that in the magnetic field. However, such a model cannot explain why the measured magnetic field strengths are always close to the value for equipartition between relativistic *electrons* and magnetic field, unless the mechanism for achieving equipartition

requires timescales longer than the lobe lifetimes for protons but not electrons. The results of our survey of FRII radio lobes support the conclusions of our earlier papers on smaller samples of sources (Hardcastle et al. 2002; Croston et al. 2004): the presence of an energetically dominant population of protons is unlikely, because it requires that the magnetic field energy density tends to be similar to the electron energy density rather than the conjectured overall energy density in relativistic particles.

6. Conclusions

Our study of the X-ray emission from the lobes of FRII radio galaxies and quasars has shown that they can be magnetically dominated by at least a factor of 2; however, > 70 percent of the sample are at equipartition or electron dominated. There is a reasonably narrow distribution of R values, where R is the ratio of observed to predicted emission from CMB IC from synchrotron-emitting electrons at equipartition. The distribution peaks at $R \sim 2$, which corresponds to magnetic field strengths within 35 percent of the equipartition value, or electron dominance (U_e/U_b) by a factor of ~ 5 . That the distribution is narrow and close to the expectation for equipartition between relativistic electrons and magnetic field shows that an energetically dominant proton population in FRII radio sources is unlikely. The distribution of apparent R values differs for narrow-line radio galaxies and broad-line objects (broad-line radio galaxies and quasars); this is due in part to projection effects, but may also be caused by worse systematic uncertainties for more distant objects. We argue that IC scattering of infrared and optical photons from the nucleus is unlikely to be the dominant X-ray emission process in the majority of radio galaxies and quasars, although it may play some rôle in smaller objects.

We thank the referee for helpful comments. We gratefully acknowledge support from PPARC (studentship for JHC and research assistantship for EB) and the Royal Society (research fellowship for MJH). This work was partially supported by NASA grant GO3-4132X.

The National Radio Astronomy Observatory is a facility of the National Science Foundation operated under cooperative agreement by Associated Universities, Inc.

A. Comparison of results for sources previously presented by other authors

In this section, we briefly discuss the lobe emission from the individual sources for which previously published results exist and compare our results with those of other authors.

A.1. 3C 9

Fabian et al. (2003) discuss the X-ray emission from this source, attributing it to inverse-Compton scattering of the CMB; however, they do not carry out a detailed calculation, and do not separate the X-ray emission from the eastern radio components (likely to be jet-related) and the western lobe, which we analysed above. Our results are in rough agreement with their less detailed analysis.

A.2. 3C 179

Sambruna et al. (2002) discuss the *Chandra* observation of 3C 179 in the context of a survey of jets studied with *HST* and *Chandra*. Their Fig. 1 shows a smoothed image of the X-ray emission; however, their choice of greyscale means that the lobe-related emission does not show up in the image, which emphasizes the jet and hotspot emission. Our 0.5 – 5.0 keV image (Fig. 1) excludes higher energy background counts included in their image (which used a larger energy range), and shows clearly an excess of counts associated with both lobes. Sambruna et al. do not mention the presence of this emission.

A.3. 3C 207

The *Chandra* observation of 3C 207 was presented by Brunetti et al. (2002). We measured only 25 0.5-5 keV counts using background subtraction at the same distance from

the nucleus, whereas they were able to fit a spectrum with 9 bins. In their discussion of background subtraction they argue that the choice of background region is not important as the *Chandra* background is extremely low; this suggests that they have not subtracted off the component of background from the wings of the PSF, which is important, as can be seen from their smoothed image. They list several reasons why they believe that IC scattering of the CMB is not the dominant process. They argue that no emission is seen from the western lobe, which is of similar radio luminosity and size to the eastern one; however, as the source is of small angular size, and the western lobe is dominated by jet emission, it is not possible to obtain a strong upper limit on its lobe-related X-ray emission, particularly in the presence of high background due to AGN emission. Brunetti et al. argue that the X-ray spectral index is flatter than the radio spectral index; however, firstly there do not appear to be sufficient counts to constrain the spectral index, and secondly they consider only the high frequency spectral index, whereas it is lower energy electrons that will scatter the CMB and the nuclear emission. We obtained an R value of 3 for the western lobe of 3C 207 (the intrinsic value may be lower due to projection, see above). It is therefore possible that some contribution to the X-ray flux comes from the IC/nuclear process as argued by Brunetti et al. (2002), but it appears that CMB IC can explain a significant fraction of the observed emission if the lobe is near equipartition, or all of the X-rays if the lobe is modestly electron-dominated or at a small angle to the line of sight.

A.4. 3C 219

Comastri et al. (2003) present the *Chandra* observation of 3C 219 and attribute the lobe-related emission to inverse-Compton scattering of the CMB and nuclear AGN photons. Our spectral results for the northern lobe are consistent with the values they obtain for the entire source. However, their quoted flux is approximately twice our measured total flux from both lobes. This is probably due to their choice of spectral extraction region, which does not exclude the jet or northern hotspot regions. Additionally, they do not specify their choice of background region: if it is off-axis, then their spectrum could contain significant AGN contamination. We obtain a comparable flux to their measured value if we use a large elliptical extraction region that includes the jet and northern hotspot, and use an off-source background region. We believe that our choice of extraction regions is preferable, as our regions follow the radio structure more closely, and because our background region, at the same distance from the core as the source regions, will remove contamination from the AGN and hot-gas environment. Therefore, we disagree with their conclusions that the lobes are electron-dominated by up to a factor of 100, and find that this factor is more than an order of magnitude lower.

A.5. 3C 265

Bondi et al. (2004) present the results of an analysis of the *Chandra* observation of 3C 265. They interpret the origin of the X-ray emission as IC scattering of AGN photons; however, our results show that CMB and SSC IC emission in an equipartition field can account for $> 1/3$ of the observed X-ray emission. It is nevertheless possible that IC/nuclear scattering makes a significant contribution to the flux from the eastern lobe, thought to be pointing away from us. To test this, we carried out similar calculations for this source to those for the eastern lobe of 3C 284 presented by Croston et al. (2004).

To model the illuminating flux, we used the infrared measurements (at 4.5, 6.7 and 12.0 μm) for 3C 265 of Siebenmorgen et al. (2004), extrapolating to a frequency range of 4×10^{12} to 10^{15} Hz. In order to model the shape of the spectrum at lower frequencies, we scaled the lower frequency spectrum for 3C 295 (Meisenheimer et al. 2001) to a value appropriate for the normalization of 3C 265’s infrared spectrum. We used the same parameters for the electron energy spectrum as in the analysis of Section 3, with γ_{min} of 10, so that the predicted flux is an upper limit on the contribution from IC/nuclear. We find that the contribution to the predicted 1-keV flux density from IC scattering of this photon field to be less than 0.03 nJy for all choices of inclination angle. Therefore, if the infrared emission is isotropic, this process cannot account for the observed flux level. In order to produce the additional X-ray flux (the observed excess of 1.7 nJy above the CMB IC prediction; see Table 7), the luminosity of the quasar as seen by the lobes would have to be ~ 60 times more luminous than the isotropic luminosity, so that a beam of small opening angle would be required. This more luminous photon field, if symmetric on each side of the source, would also produce a significant flux from the western radio lobe (e.g., ~ 1 nJy for the most probable angle of 69°), so that IC/nuclear scattering in an equipartition magnetic field cannot explain the observed fluxes. Another argument against illumination from a narrow cone of infrared emission is the lack of evidence for differences in the infrared properties of narrow-line and broad line radio galaxies (Meisenheimer et al. 2001). Finally, the IC/nuclear model predicts a steep decrease in the X-ray flux with distance from the nucleus; this is not seen in the X-ray data. The asymmetry in X-ray-to-radio flux is therefore more plausibly explained by a difference in the relative magnetic field strength of the two lobes, perhaps due to their different sizes.

There are several differences between our method and that of Bondi et al., which may explain our different conclusions as to the dominant photon population. Our X-ray observational measurements appear to be in reasonable agreement; however, from our L-band radio map we measure a much smaller flux ratio between the two lobes than that quoted by Bondi et al. (a ratio of 2.7 between the east and west lobes). We also use a concordance model cosmology, whereas Bondi et al. use a value of $q_0 = 0.5$; this has a significant effect on the

volumes and the CMB energy density. The different radio measurements and cosmology may explain why our value for the equipartition magnetic field (2.4 nT) is a factor of two below theirs. We used an illuminating spectrum based directly on the infrared measurements of Siebenmorgen et al. (2004) for 3C 265, which gives an integrated luminosity just below the lower limit of the range quoted by Bondi et al. In contrast, they use a value close to the upper limit of their quoted range. Finally, we assumed that the illuminating source is isotropic, as supported by arguments from unified models (see above). We believe our choice of cosmology is more appropriate, and our parametrization of the illuminating source is based directly on infrared measurements, and so we conclude that, in contrast to the findings of Bondi et al., IC from CMB photons in a near-equipartition field ($B \sim 0.6B_{eq}$) can explain the observed X-ray flux, and that the contribution from IC/nuclear is not dominant in this source.

A.6. 3C 281

Crawford and Fabian (2003) presented the *Chandra* observation of 3C 281 and attributed the extended X-ray emission to the northern hotspot and environment. They mention the presence of extended soft emission along the jet axis of the four sources they observe in the context of lobe IC emission; however, they concentrated primarily on the environmental properties and did not carry out any analysis of radio-related emission. The emission they considered to be hotspot-related is not sufficiently compact or directly associated with the radio hotspot, leading Hardcastle et al. (2004) to argue that the radio-related emission is associated instead with the lobe. Crawford & Fabian found that the luminosity of the extended emission is much lower than the values estimated using *ROSAT*, which is probably due to the poorly known *ROSAT* PSF. The true group or cluster luminosity may be even lower, once the contribution from lobe-related emission is removed.

A.7. 3C 452

An in-depth study of the lobe-related emission from 3C 452 was presented by Isobe et al. (2002), including analysis of the spatial structure of electrons and magnetic field in the lobes. They attribute all of the non-thermal emission to IC scattering of the CMB and find a best-fitting power-law plus Raymond-Smith model with similar spectral parameters to those given in Table 2. They carry a simple comparison of the ratios of synchrotron radiation to X-ray IC emission and estimate that the lobes are electron dominated by a factor of 27^{+25}_{-16} . Their lower limit is roughly consistent with our estimated value of 9, which was determined using a more detailed synchrotron and inverse-Compton modelling procedure.

REFERENCES

- Aldcroft, T. L., Siemiginowska, A., Elvis, M., Mathur, S., Nicastro, F., and Murray, S. S.: 2003, *ApJ* **597**, 751
- Barthel, P. D.: 1989, *ApJ* **336**, 606
- Bell, A. R.: 1978 *MNRAS* **182**, 147
- Belsole, E., Worrall, D. M., Hardcastle, M. J., Birkinshaw, M., and Lawrence, C. R.: 2004, *MNRAS* **352**, 924
- Best, P. N.: 2004, *MNRAS* **351**, 70
- Bondi, M., Brunetti, G., Comastri, A., and Setti, G.: 2003, *New Astronomy Review* **47**, 443
- Bondi, M., Brunetti, G., Comastri, A., and Setti, G.: 2004, *MNRAS* **354**, L43
- Brunetti, G., Bondi, M., Comastri, A., and Setti, G.: 2002, *A&A* **381**, 795
- Brunetti, G., Cappi, M., Setti, G., Feretti, L., and Harris, D. E.: 2001, *A&A* **372**, 755
- Brunetti, G., Setti, G., and Comastri, A.: 1997, *A&A* **325**, 898
- Carilli, C. L., Perley, R. A., Dreher, J. W., and Leahy, J. P.: 1991, *ApJ* **383**, 554
- Celotti, A. and Fabian, A. C.: 1993, *MNRAS* **264**, 228
- Clarke, D. A., Bridle, A. H., Burns, J. O., Perley, R. A., and Norman, M. L.: 1992, *ApJ* **385**, 173
- Comastri, A., Brunetti, G., Dallacasa, D., Bondi, M., Pedani, M., and Setti, G.: 2003, *MNRAS* **340**, L52
- Crawford, C. S. and Fabian, A. C.: 2003, *MNRAS* **339**, 1163
- Crawford, C. S., Fabian, A. C., Sanders, J. S., and Ettori, S.: 2003, *New Astronomy Review* **47**, 239
- Croston, J. H., Birkinshaw, M., Hardcastle, M. J., and Worrall, D. M.: 2004, *MNRAS* **353**, 879
- Dickey, J. M. and Lockman, F. J.: 1990, *ARA&A* **28**, 215
- Donahue, M., Daly, R. A., and Horner, D. J.: 2003, *ApJ* **584**, 643

- Fabian, A. C., Celotti, A., and Johnstone, R. M.: 2003, *MNRAS* **338**, L7
- Fanaroff, B. L. and Riley, J. M.: 1974, *MNRAS* **167**, 31P
- Giovannini, G., Feretti, L., Venturi, T., Lara, L., Marcaide, J., Rioja, M., Spangler, S. R., and Wehrle, A. E.: 1994, *ApJ* **435**, 116
- Hardcastle, M. J., Birkinshaw, M., Cameron, R. A., Harris, D. E., Looney, L. W., and Worrall, D. M.: 2002, *ApJ* **581**, 948
- Hardcastle, M. J., Birkinshaw, M., and Worrall, D. M.: 1998a, *MNRAS* **294**, 615
- Hardcastle, M. J., Birkinshaw, M., and Worrall, D. M.: 2001, *MNRAS* **323**, L17
- Hardcastle, M. J., Harris, D. E., Worrall, D. M., and Birkinshaw, M.: 2004, *ApJ* **612**, 729
- Hardcastle, M. J. and Worrall, D. M.: 2000, *MNRAS* **319**, 562
- Hardcastle, M. J., Worrall, D. M., and Birkinshaw, M.: 1998b, *MNRAS* **296**, 1098
- Harris, D.: 2004, in *From Clark Lake to the Long Wavelength Array: Bill Erickson's Radio Science*, Eds. Kassim, Perez, Junor, and Henning. To be published in Astron. Soc. Pacific conference series.
- Homan, D. C. and Wardle, J. F. C.: 1999, *AJ* **118**, 1942
- Isobe, N., Tashiro, M., Makishima, K., Iyomoto, N., Suzuki, M., Murakami, M. M., Mori, M., and Abe, K.: 2002, *ApJ* **580**, L111
- Kataoka, J., Edwards, P., Georganopoulos, M., Takahara, F., and Wagner, S.: 2003a, *A&A* **399**, 91
- Kataoka, J., Leahy, J. P., Edwards, P. G., Kino, M., Takahara, F., Serino, Y., Kawai, N., and Martel, A. R.: 2003b, *A&A* **410**, 833
- Kataoka, J. and Stawarz, L.: 2005, *ApJ in press (astro-ph/0411042)*
- Kino, M. and Takahara, F.: 2004, *MNRAS* **349**, 336
- Kraft, R., Hardcastle, M., Worrall, D., and Murray, S.: 2005, *ApJ in press (astro-ph/0501031)*
- Kraft, R. P., Vázquez, S. E., Forman, W. R., Jones, C., Murray, S. S., Hardcastle, M. J., Worrall, D. M., and Churazov, E.: 2003, *ApJ* **592**, 129

- Laing, R. A., Jenkins, C. R., Wall, J. V., and Unger, S. W.: 1994, in *Astronomical Society of the Pacific Conference Series*, pp 201–+
- Leahy, J. P., Bridle, A. H., and Ström, R. G.: 1998
- Leahy, J. P. and Perley, R. A.: 1991, *AJ* **102**, 537
- Leahy, J. P. and Perley, R. A.: 1995, *MNRAS* **277**, 1097
- Liu, R. and Pooley, G.: 1991, *MNRAS* **249**, 343
- Meisenheimer, K., Haas, M., Müller, S. A. H., Chini, R., Klaas, U., and Lemke, D.: 2001, *A&A* **372**, 719
- Meisenheimer, K., Yates, M. G., and Roeser, H.-J.: 1997, *A&A* **325**, 57
- Overzier, R., Harris, D., Carilli, C., Pentericci, L., Röttgering, H., and Miley, G.: 2005, *A&A in press (astro-ph/0412026)*
- Reynolds, C. S., Brenneman, L. W., and Stocke, J. T.: 2004, *ArXiv Astrophysics e-prints*
- Sambruna, R. M., Maraschi, L., Tavecchio, F., Urry, C. M., Cheung, C. C., Chartas, G., Scarpa, R., and Gambill, J. K.: 2002, *ApJ* **571**, 206
- Siebenmorgen, R., Freudling, W., Krügel, E., and Haas, M.: 2004, *A&A* **421**, 129
- Urry, C. M. and Padovani, P.: 1995, *PASP* **107**, 803
- Wardle, J. F. C., Homan, D. C., Ojha, R., and Roberts, D. H.: 1998, *Nature* **395**, 457
- Wilson, A. S., Young, A. J., and Shopbell, P. L.: 2000, *ApJ* **544**, L27
- Worrall, D. M., Birkinshaw, M., Hardcastle, M. J., and Lawrence, C. R.: 2001, *MNRAS* **326**, 1127